Prediction of manganese trihalides as two-dimensional Dirac half-metals

Qilong Sun[*] and Nicholas Kioussis[†]

Department of Physics and Astronomy, California State University, Northridge, California 91330, USA

The recent discovery of intrinsic ferromagnetism in two-dimensional (2D) van der Waals crystals down to the monolayer limit has sparked intense interest due to their potential applications in spintronics. Here, using first-principles calculations we predict that the 2D pristine MnX_3 (X = F, Cl, Br, I) is a family of intrinsic Dirac half-metals characterized by a band structure with an unusually large gap in one spin channel and a Dirac cone in the other with carrier mobilities comparable to those in graphene. We demonstrate that the MnX_3 are dynamically and thermodynamically stable up to high temperatures, and exhibit large magnetic moments of about $4\,\mu_B$ per Mn^{3+} ion, high Curie temperatures, and large in-plane magnetic anisotropy energy. In addition, the gap opening induced by the spin-orbit coupling drives the lighter systems into the quantum anomalous Hall state. The combination of these unique properties renders this class of 2D ferromagnets a promising platform for high efficiency spintronic applications.

I. INTRODUCTION

Spintronics, involving transmission and storage of information by manipulating the spin degrees of freedom, has sparked tremendous interest over the past decades, because it offers unique advantages to conventional charge-based electronic devices, such as greater data processing speed, high integration density, low power consumption, and nonvolatility [1]. Several key properties have been identified for developing new magnetic materials for spintronic devices: Room-temperature half-metallicity, large magnetocrystalline anisotropy (MCA), high Curie temperature, and high spin mobility [2,3].

Bulk half-metals (HMs), with one spin channel conducting and the other semiconducting are ideal spintronic materials which exhibit 100% spin polarization [4–6]. However, in order to preserve the half-metallicity at room temperature the band gap of one spin channel should be wide enough to prevent thermally induced spin-flip transitions. An additional challenge is to sustain the half-metallic character in ultrathin HM films [7].

Another distinct class of materials, referred to as "Dirac materials" [8], such as graphene [9], topological insulators [10], Dirac [11], and Weyl semimetals [12], is characterized by low-energy fermionic excitations that behave as massless Dirac particles with linear dispersion. The combination of the intriguing properties of the HM and the Dirac materials could give rise to yet another exotic state of matter, the so-called Dirac half-metal (DHM), characterized by a band structure with a gap in one channel but a Dirac cone in the other [13,14]. Furthermore, if the DHM possesses strong spin-orbit coupling (SOC), it can trigger a gap opening in one spin channel and drive in turn the system in the quantum anomalous Hall effect (QAH) state. Recent first-principles electronic structure calculations predicted that the bulk crystal structure of MnF_3, in the hexagonal $R\bar{3}c$ space group (No. 167), is a DHM [15]. Nevertheless,

the multiple Dirac cones do not persist in ultrathin (≈ 1 nm) MnF_3 films irrespective of the surface orientation [16].

While there has been tremendous progress in the field of 2D materials displaying a broad range of electronic and optical properties [9,17,18], most of them in the pristine form are nonmagnetic, thus limiting their applications in spintronics. Although magnetism can be introduced by dopants and defects [13,19], a long-range magnetic order has rarely been observed experimentally in 2D materials. Interestingly, during the past year two teams have observed clear signatures of magnetism in 2D $CrGeTe_3$ [20] and CrI_3 [21] van der Waals materials down to the monolayer limit. However, both these 2D materials are ferromagnetic insulators with low Curie temperatures of 45 K and 90 K, respectively. Yet, no 2D DHM pristine material has been experimentally synthesized. Consequently, there is an intense current effort on identifying 2D materials to realize such an exotic state that will also satisfy the above material requirements.

In this article, employing *ab initio* electronic structure calculations we predict that monolayer manganese halides, MnX_3 (X = F, Cl, Br, I), are DHM that are dynamically and thermodynamically stable up to high temperatures. Consequently, this family of pristine DHM could be synthesized experimentally in 2D hexagonal structures. Furthermore, we demonstrate that the MnX_3 exhibit relatively high Curie temperatures and giant in-plane magnetic anisotropy energy. In addition, the SOC opens a global band gap in the lighter systems, giving rise to a topologically nontrivial Chern-insulating state. The combination of these properties renders the MnX_3 family a promising platform for future applications in electronics and spintronics.

II. METHODOLOGY

Density functional theory (DFT) calculations were carried out using the Vienna *ab initio* simulation package (VASP) [22,23]. The pseudopotential and wave functions are treated within the projector-augmented wave (PAW) method [24]. Structural relaxations were carried out using the generalized gradient approximation as parametrized by Perdew *et al.* [25].
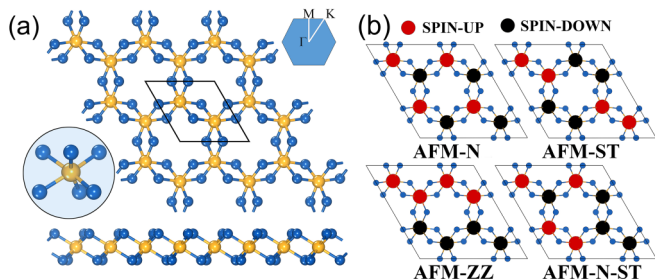
---

[*]qilong.sun@csun.edu

[†]nick.kioussis@csun.edu

FIG. 1. (a) Top and side views of the 2D MnX$_3$ crystal structure with the unit cell, where the yellow and blue spheres denote the Mn and X atoms, respectively. The MnX$_6$ octahedron with each Mn^{3+} ion coordinated to six X$^-$ ions and the hexagonal BZ. (b) Top view of various AFM spin configurations: AFM-Néel (AFM-N), AFM-stripy (AFM-ST), AFM-zigzag (AFM-ZZ), and mixed AFM-N-ST, where the red (black) circles denote the up (down) spins.

The plane-wave cutoff energy was set to 500 eV and a $9 \times 9 \times 1$ k mesh was used in the Brillouin zone (BZ) sampling for the relaxation calculations. The band structure was calculated using (i) the DFT+U approach [26] (U=3.9 eV) to treat the strong correlations of the Mn d electrons and (ii) the more accurate Heyd-Scuseria-Ernzerhof (HSE06) [27] functional. For the MCA calculations, the SOC was included with a $31 \times 31 \times 1$ k-point mesh. For the phonon calculations the VASP and PHONOPY [28] codes were employed with a $3 \times 3 \times 1$ 72-atom supercell to determine the dynamical matrix.

III. RESULTS AND DISCUSSION

Equilibrium structural and magnetic properties. The crystal structure of the MnX$_3$ monolayer, shown in Fig. 1(a), consists of a plane of Mn atoms forming a honeycomb lattice and sandwiched between two X atomic planes, with two Mn and six X atoms per (1×1) unit cell, similar to that of CrI$_3$ [21]. The Mn ions are surrounded by six first-nearest-neighbor halogens arranged in an edge sharing distorted octahedra, shown in Fig. 1(a). In sharp contrast to the crystal structure in Ref. [15] where two Mn ions are bonded by a single anion, two Mn^{3+} in Fig. 1(a) are bonded by two anions. Consequently, the crystal structure in Fig. 1(a) is dramatically distinct than any of the surface orientations of bulk MnF$_3$.

We have carried total-energy spin-polarized calculations of the $2 \times 2 \times 1$ unit cell of the ferromagnetic (FM) and various antiferromagnetic (AFM) phases, such as the AFM-Néel (AFM-N), the AFM-zigzag (AFM-ZZ), the AFM-stripy (AFM-SR), and the mixed AFM-N-ST, respectively, shown in Fig. 1(b). We find (Table I) that the optimized FM is the ground state for all MnX$_3$ and that the next highest-energy configuration is the AFM-ZZ for X = Cl, Br, and I and the AFM-N-ST for X = F. Table I lists values of the equilibrium lattice constants, the Mn-Mn and Mn-X bond lengths, the X-Mn-X angle, the Mn magnetic moments, and cohesive energies for the FM phase. We also list values of the energy differences, between the most likely AFM-ZZ and AFM-N-S and the FM ground state. As expected, the lattice constant, the Mn-Mn and Mn-X bond lengths increase as the halogen anion's ionic radius increases. For the MnF$_3$ ML, the Mn-F bond length of 1.96 Å is close to the value of 1.93 Å in bulk β-MnF$_4$, implying strong

TABLE I. Calculated equilibrium lattice constant, bond lengths of Mn-X and Mn-Mn, cohesive energy, angle of the X-Mn-X bond, cohesive energy, magnetic moment of Mn^{3+}, and MCA per unit area, respectively, for the FM ground state. We also list values of the energy difference between the FM ground state and the AFM-ZZ and AFM-N-ST states, respectively, of the $2 \times 2 \times 1$ unit cell.

	MnF$_3$	MnCl$_3$	MnBr$_3$	MnI$_3$
a(Å)	5.36	6.21	6.58	7.08
$d_{\mathrm{Mn-X}}$ (Å)	1.96	2.38	2.55	2.77
$d_{\mathrm{Mn-Mn}}$ (Å)	3.09	3.58	3.83	4.08
$\angle$Mn-X-Mn (°)	104.29	97.44	96.10	94.81
E_{coh} (eV/atom)	−4.33	−3.10	−2.70	−2.31
μ (μ_B)	3.92	4.08	4.18	4.27
$E_{\mathrm{AFM-ZZ}} - E_{\mathrm{FM}}$ (meV)	273	212	248	250
$E_{\mathrm{AFM-N-ST}} - E_{\mathrm{FM}}$ (meV)	115	269	430	436
MCA (erg/cm^2)	−0.013	−0.46	−8.71	−11.86

chemical bonding. Similarly, the cohesive energy decreases with an increasing atomic number of the halogen due to the decreasing electronegativity of the halogen anion.

The magnetic moment per Mn atom of the FM phase, also listed in Table I, increases from 3.92 μ_B in MnF$_3$ to 4.27 μ_B in MnI$_3$. The magnetic moment is consistent with the +3 oxidation state of Mn and hence the $4s^0 3d^4$ electronic configuration. In the octahedral environment of the six halogens the $3d$ energy split into a higher-energy e_g doublet and a lower-energy t_{2g} triplet, resulting in a spin $S = 2$ $t_{2g}^3 e_g^1$ electronic configuration for the Mn^{+3} ion according to the Hund's rule coupling. This is similar to the 2D organometallic honeycomb framework with different embedded transition metals. The electron localization function for MnF$_3$ displayed in Fig. 4S(b) (Supplemental Material [29]), shows strong localization of the electron density around the metal cations and halogen anions representative of Mn-X ionic bonding.

The MCA per unit area A is, MCA = $[E_{[100]} - E_{[001]}]/A$, where $E_{[100]}$ and $E_{[001]}$ are the total energies with magnetization along the [100] and [001] directions, respectively. The values of MCA, listed in Table I, show that the MCA < 0 indicating the in-plane magnetization orientation in all MnX$_3$'s. Furthermore, the |MCA| increases with increasing halogen size. The value of −0.46 erg/cm^2 in MnCl$_3$ is comparable to that of −0.56 erg/cm^2 in the ultrathin Au/FeCo/MgO heterostructure [30] for MRAM applications. More importantly, the MCA values of 8.71 erg/cm^2 and 11.9 erg/cm^2 in MnBr$_3$ and MnI$_3$, respectively, are about an order of magnitude higher than that of 1.4 erg/cm^2 in Ta/FeCo/MgO MRAM nanojunctions. The giant MCA values presumably arise from the strong SOC of the heavier X = Br, I, suggesting that introduction of heavy elements in transition metal-based films, may be an efficient strategy in enhancing the MCA.

Dynamical and thermal stability. In order to corroborate the dynamical stability of the FM ground state of the 2D MnX$_3$ we have carried out both phonon calculations and *ab initio* Born Oppenheimer molecular dynamics (BOMD) simulations. The phonon dispersions of the MnX$_3$, shown in Fig. 2(a), exhibit similar overall shape with the phonon frequencies softening with increasing mass of X. The absence of imaginary
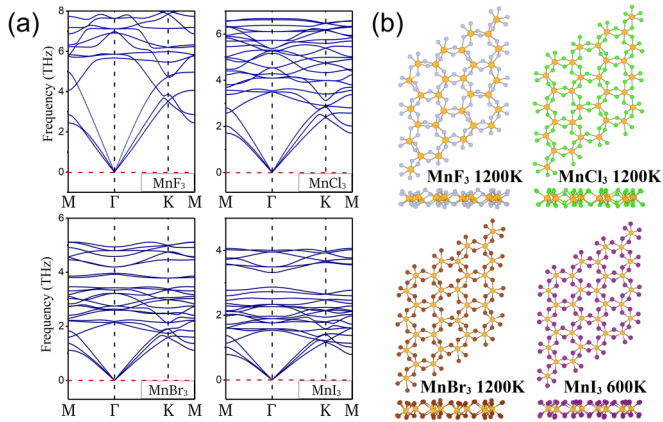
FIG. 2. (a) Calculated phonon dispersion curves of the 2D MnX$_3$. (b) Top and side views of atomic structure snapshots from BOMD simulations at 1200 K or 900 K.

frequencies confirms the dynamical stability of all MnX$_3$ monolayers. Figure 2(b) and Supplemental Material, Fig. 1S [29], show the snapshots of the MnX$_3$ atomic configurations after annealing for 10 ps at different temperatures of 300, 600, 900, and 1200 K, respectively. One can clearly see that the 2D monolayers retain their honeycomb atomic structures up to 1200 K for MnF$_3$, MnCl$_3$, and MnBr$_3$, and up to 600 K for MnBr$_3$ [see Fig. 1S(d) in Supplemental Material [29]]. This is consistent with the higher cohesive energies of the lighter MnX$_3$ systems. These results demonstrate that the 2D manganese trihalides are both dynamically and thermally stable for various room-temperature spintronic applications.
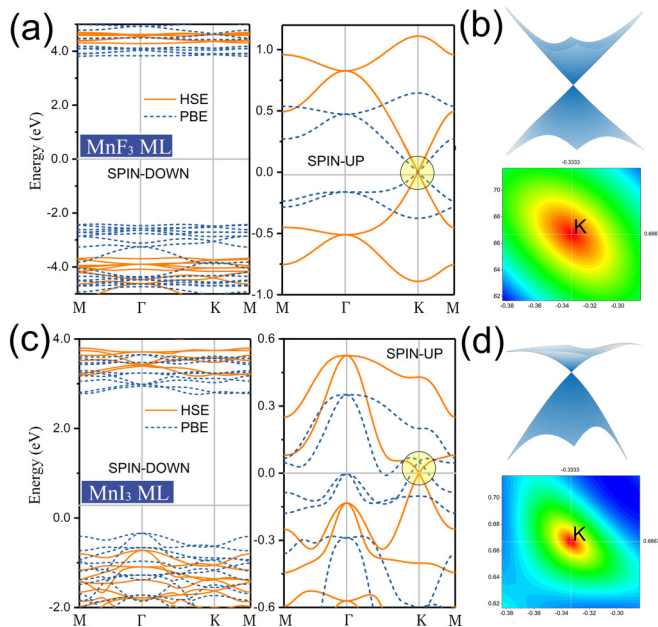

FIG. 3. (a) and (c) Minority- and majority-spin band structure of the 2D MnF$_3$ and MnI$_3$ FM phase using the DFT+U and HSE06 method. (b) and (d) 3D band structure of the Dirac cone at the K symmetry point and the corresponding projection on the BZ around the Fermi energy (set at zero).

Electronic structure. Figures 3(a) and 3(c) show the minority- and majority-spin band structures of the FM phase for the MnF$_3$ and MnI$_3$ monolayer, respectively, employing the PBE+U (orange curves) and the more accurate hybrid HSE06 (blue curves) functional. Similar band structures for the MnCl$_3$ and MnBr$_3$ are displayed in Figs. 2S(a) and 2S(c) in Supplemental Material [29]. These calculations reveal that all MnX$_3$ exhibit two fascinating properties which are independent of the exchange correlation functional: (1) The minority-spin channel is an insulator with an unusually large gap, and (2) the majority-spin channel exhibits Dirac cones at the three high-symmetry K points at the Fermi level (E_F) for X = F, Cl, Br. While the Dirac cone is in the vicinity of E_F for the heaviest MnI$_3$ at the PBE+U level, the HSE06 functional shifts it at the E_F. Consequently, we predict that the 2D MnX$_3$ are intrinsic DHMs. The PBE+U values of the band gap of the minority-spin channel are 6.3 eV, 4.33 eV, 3.85 eV, and 3.10 eV for the MnF$_3$, MnCl$_3$, MnBr$_3$, and MnI$_3$, respectively. The PBE functional underestimates the gap by about 20% compared to the corresponding HSE06 values of 7.94 eV, 5.42 eV, 4.79 eV, and 3.89 eV, respectively. The HSE06 values of the Fermi velocities of the Dirac electrons are 3.83×10^5, 2.40×10^5, and 2.31×10^5 m/s for MnF$_3$, MnCl$_3$, and MnBr$_3$, respectively, close to the value of 8×10^5 m/s in graphene. For MnI$_3$ the Fermi velocities of the Dirac electrons and holes are 1.56×10^5 m/s and 3.36×10^5 m/s, respectively. The combination of 100% spin polarization and massless Dirac fermions renders this family a natural candidate for future applications in spintronics and optoelectronics.

The three-dimensional (3D) majority-spin band profiles around E_F near K are shown in Figs. 3(b) and 3(d) for MnF$_3$ and MnI$_3$, and in Figs. 2S(b) and 2S(d) in Supplemental Material [29] for MnCl$_3$ and MnBr$_3$, respectively. With an increasing atomic number of the halogen, the Dirac cone of the conduction band minimum becomes flatter while there is no significant change of the cone of the valence band maximum. The corresponding projection of the Dirac cones on the 2D BZ around the Fermi level are shown in Figs. 3(b) and 3(d).

The atom- and orbital-resolved majority-spin band structures obtained with the HSE06 functional are shown in Figs. 4(a) and 4(b) for X = F, I, and in Figs. 3S(a) and 3S(b) in Supplemental Material [29] for X = Cl, Br, respectively. Over-all, we find that the linearly dispersive majority-spin electronic bands at the Fermi energy arise from hybridization primary of the Mn-derived d_{xz} and d_{yz} (and to a smaller extent of $d_{x^2-y^2}$) states with the halogen-derived in-plane p_x and p_y states. The relative strength of the X-$p_{x,y}$ to the Mn-$d_{xz,yz}$ contribution increases as the halogen atomic size increases down the group, where the Dirac cone is mainly composed of Mn-d derived states in MnF$_3$ and of X-p states in MnI$_3$. The valence and conduction bands of the Dirac cone are composed mainly of anion-p_x and -p_y derived states, respectively. The low-energy Dirac cone Mn-d-derived states in MnF$_3$ are in sharp contrast to the corresponding p-derived states in graphene. In addition, the weak hybridization of the in-plane halogen-$p_{x,y}$ Dirac states with the underlying substrates will presumably preserve the Dirac cone, as opposed to the strong out-of-plane $\pi(p_z)$ hybridization of graphene bonds with substrates.

Effect of spin-orbit coupling. Figure 4S(a) in Supplemental Material [29] shows the band structure of MnX$_3$ determined by the HSE06 functional in the presence of SOC. The inclusion of
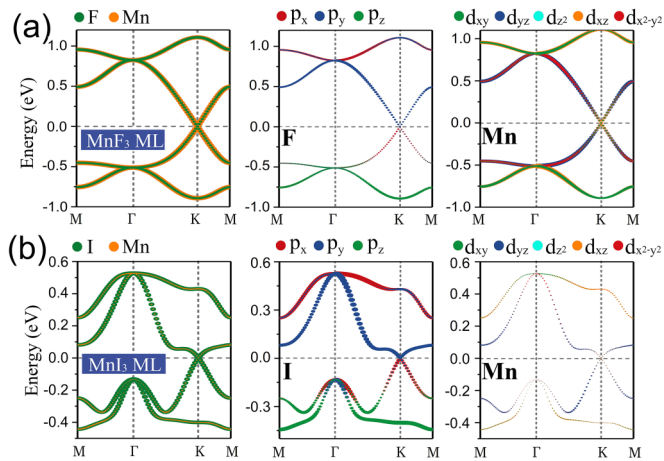
FIG. 4. Energy and **k** contribution of atom-resolved (left panel), halogen-p-resolved (middle panel), and Mn-d-resolved (right panel) to the majority-spin bands for (a) MnF$_3$ and (b) MnI$_3$ using the HSE06 functional. The color intensity denotes the amplitude of the atom- and/or orbital-resolved character.

SOC triggers a small gap opening of ∼3–10 meV at the high symmetry K point indicating that the 100% spin polarization will be maintained at room temperature. Remarkably, the linear band dispersion of the majority spin channel is also preserved in the presence of SOC for the lighter halogens (X = F, Cl, and Br). On the other hand, the large SOC of the iodine induces (i) a gap opening of ∼91 meV at K, and (ii) splits the doubly degenerate I-derived $p_{x,y}$ states at ∼0.15 eV below E_F at Γ [see Fig. 4(b)] into one band ∼0.1 eV above E_F and the other ∼ 0.3 eV below E_F, thus preserving the half-metallicity of MnI$_3$.

To identify the topological properties of the gapped state of the lighter MnX$_3$, we have calculated the Chern number of MnBr$_3$, which exhibits the largest gap. We have employed the Wannier charge centers approach [31], where the maximally localized Wannier functions were constructed from the first-principles calculations including SOC using the WANNIER90 package [32]. The Chern number for the MnBr$_3$ monolayer is calculated from the evolution of the hybrid Wannier charge centers (HWCCs) during a time-reversal pumping process [33,34]. The Chern number, $C = \frac{1}{ea}[P_e^h(2\pi) - P_e^h(0)]$, where a is the lattice constant, $P_e^h(k_y) = e \sum_n \bar{x}_n(k_y)$ is the hybrid electronic polarization, and the HWCC, $\bar{x}_n(k_y)$, is a smooth function of k_y for $k_y \in [0, 2\pi]$. Namely, the Chern number can be viewed as the number of electronic charges pumped across one unit cell in the course of a cycle [35]. We find an odd Chern number, $C = -1$, for MnBr$_3$, indicating that it is a QAH insulator with a topological nontrivial gap. To corroborate this result we have calculated the band structures of the zizzag and armchair edges of the MnBr$_3$ ribbon, which are displayed in Fig. 5(a). The emergence of a single chiral topologically protected gapless edge state near E_F connecting the 2D valence and conduction bands is consistent with the calculated Chern number. Thus, we predict than MnF$_3$, MnCl$_3$, and MnBr$_3$ provide a promising platform for exploring the QAH effect at ∼60–100 K, which is three orders of magnitude higher than the temperature of 100 mK at which the QAH was recently observed in Cr-doped Bi$_2$Se$_3$ films [36].
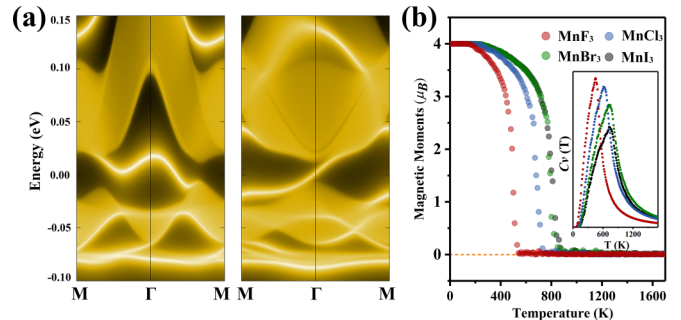

FIG. 5. (a) Band structure of the zigzag (left) and the armchair (right) edges of the MnBr$_3$ ribbon, with the edge states connecting the 2D valence and conduction bands. (b) Temperature variation of the Mn^{3+} magnetic moment for the 2D MnX$_3$. (Inset) Temperature variation of the heat capacity.

Thermodynamic properties. Since the values of the X-Mn-X angle, listed in Table I, are close to 90° the superexchange interaction between two nearest-neighbor (NN) Mn atoms mediated by X are expected to be FM and dominant (the direct AFM exchange interactions are weak due to the large Mn-Mn distance). The exchange interaction parameters J_{ij} are determined by expressing the DFT total energies of the various FM and AFM configurations to the Heisenberg spin Hamiltonian, $H = -\sum_{i,j} J_{i,j} \vec{S}_i \cdot \vec{S}_j$, defined on a honeycomb lattice, where $|\vec{S}| = 2$. The second- and third-NN exchange interactions are smaller than the first-NN interaction J_1, which increases from 3.8 meV in MnF$_3$ to 10 meV in MnI$_3$. Using the DFT-derived exchange interactions, we have determined the Curie temperature T$_c$, using Metropolis Monte Carlo simulations of the 100×100 2D honeycomb lattice with periodic boundary conditions. The temperature variation of the Mn^{3+} magnetic moment for the MnX$_3$ is shown in Fig. 5(b). We find that T$_c$ increases from 450 K in MnF$_3$ to 720 K in MnI$_3$, which are higher than that of ≈66 K in CrI$_3$. The inset shows the temperature variation of the specific heat which peaks at T$_c$.

IV. CONCLUSION

In summary, we predict that the 2D pristine manganese trihalides is a family of intrinsic Dirac half-metals which exhibits many unique properties, including 100% spin polarization, massless Dirac fermions with high carrier mobility, large magnetic moments, high Curie temperatures, and large in-plane magnetic anisotropy. Consequently, they meet many requirements of high-efficiency spintronic applications. We demonstrate that the MnX$_3$ are dynamically and thermodynamically stable up to high temperatures and hence could be synthesized experimentally by an exfoliation process commonly employed in other 2D van der Waal crystals. Lastly, in contrast with conventional FM films which interact strongly with the underlying substrates, the electronic and magnetic properties of these 2D van der Waals DSMs can remain on substrates.

[1] S. A. Wolf, D. D. Awschalom, R. A. Buhrman, J. M. Daughton, S. von Molnar, M. L. Roukes, A. Y. Chtchelkanova, and D. M. Treger, Spintronics: A spin-based electronics vision for the future, Science **294**, 1488 (2001).

[2] A. Hirohata, H. Sukegawa, H. Yanagihara, I. Žutic, T. Seki, S. Mizukami, and R. Swaminathan, Roadmap for emerging materials for spintronic device applications, IEEE T. Magn. **51**, 1 (2015).

[3] Y. Sun, Z. Zhuo, X. Wu, and J. Yang, Room-temperature ferromagnetism in two-dimensional Fe$_2$Si nanosheet with enhanced spin-polarization ratio, Nano Lett. **17**, 2771 (2017).

[4] R. A. de Groot, F. M. Mueller, P. G. van Engen, and K. H. J. Buschow, New Class of Materials: Half-Metallic Ferromagnets, Phys. Rev. Lett. **50**, 2024 (1983).

[5] J.-H. Park, E. Vescovo, H.-J. Kim, C. Kwon, R. Ramesh, and T. Venkatesan, Direct evidence for a half-metallic ferromagnet, Nature (London) **392**, 794 (1998).

[6] P. Mavropoulos, M. Ležaić, and S. Blügel, Half-metallic ferromagnets for magnetic tunnel junctions by *ab initio* calculations, Phys. Rev. B **72**, 174428 (2005).

[7] I. Galanakis, Surface properties of the half-and full-Heusler alloys, J. Phys: Condens. Matter **14**, 6329 (2002).

[8] T. O. Wehling, A. M. Black-Schaffer, and A. V. Balatsky, Dirac materials, Adv. Phys. **63**, 1 (2014).

[9] K. S. Novoselov, A. K. Geim, S. V. Morozov, D. Jiang, Y. Zhang, S. V. Dubonos, I. V. Grigorieva, and A. A. Firsov, Electric field effect in atomically thin carbon films, Science **306**, 666 (2004).

[10] M. Z. Hasan and C. L. Kane, Topological insulators, Rev. Mod. Phys. **82**, 3045 (2010).

[11] Z. K. Liu, J. Jiang, B. Zhou, Z. J. Wang, Y. Zhang, H. M. Weng, D. Prabhakaran, S-K. Mo, H. Peng, P. Dudin, T. Kim, M. Hoesch, Z. Fang, X. Dai, Z. X. Shen, D. L. Feng, Z. Hussain, and Y. L. Chen, A stable three-dimensional topological Dirac semimetal Cd$_3$As$_2$, Nat. Mater. **13**, 677 (2014).

[12] X. Wan, A. M. Turner, A. Vishwanath, and S. Y. Savrasov, Topological semimetal and Fermi-arc surface states in the electronic structure of pyrochlore iridates, Phys. Rev. B **83**, 205101 (2011).

[13] Y. Li, D. West, H. Huang, Jia Li, S. B. Zhang, and W. Duan, Theory of the Dirac half metal and quantum anomalous Hall effect in Mn-intercalated epitaxial graphene, Phys. Rev. B **92**, 201403 (2015).

[14] Z. F. Wang, Z. Liu, and F. Liu, Quantum Anomalous Hall Effect in 2D Organic Topological Insulators, Phys. Rev. Lett. **110**, 196801 (2013).

[15] Y. Jiao, F. Ma, C. Zhang, J. Bell, S. Sanvito, and A. Du, A First-Principles Prediction of Spin-Polarized Multiple Dirac Rings in Manganese Fluoride, Phys. Rev. Lett. **119**, 016403 (2017).

[16] Q. Sun and N. Kioussis (private communication).

[17] K. F. Mak, K. L. McGill, J. Park, and P. L. McEuen, The valley Hall effect in MoS$_2$ transistors, Science **344**, 1489 (2014).

[18] Q. Sun, Y. Dai, Y. Ma, Na Yin, W. Wei, Lin Yu, and B. Huang, Design of lateral heterostructure from arsenene and antimonene, 2D Mater. **3**, 035017 (2016).

[19] J. Červenka, M. I. Katsnelson, and C. F. J. Flipse, Room-temperature ferromagnetism in graphite driven by two-dimensional networks of point defects, Nat. Phys. **5**, 840 (2009).

[20] C. Gong, L. Li, Z. Li, H. Ji, A. Stern, Y. Xia, T. Cao, W. Bao, C. Wang, Y. Wang, Z. Q. Qiu, R. J. Cava, S. G. Louie, J. Xia, and X. Zhang, Discovery of intrinsic ferromagnetism in two-dimensional van der Waals crystals, Nature (London) **546**, 265 (2017).

[21] B. Huang, G. Clark, E. Navarro-Moratalla, D. R. Klein, R. Cheng, K. L. Seyler, D. Zhong, E. Schmidgall, M. A. McGuire, D. H. Cobden, W. Yao, D. Xiao, P. Jarillo-Herrero, and X. Xu, Layer-dependent ferromagnetism in a Van der Waals crystal down to the monolayer limit, Nature (London) **546**, 270 (2017).

[22] G. Kresse and J. Furthmüller, Efficient iterative schemes for *ab initio* total-energy calculations using a plane-wave basis set, Phys. Rev. B **54**, 11169 (1996).

[23] G. Kresse and J. Furthmüller, Efficiency of ab-initio total energy calculations for metals and semiconductors using a plane-wave basis set, Comput. Mater. Sci. **6**, 15 (1996).

[24] P. E. Blöchl, Projector augmented-wave method, Phys. Rev. B **50**, 17953 (1994).

[25] J. P. Perdew, K. Burke, and M. Ernzerhof, Generalized Gradient Approximation Made Simple, Phys. Rev. Lett. **77**, 3865 (1996).

[26] V. I Anisimov, F. Aryasetiawan, and A. I. Lichtenstein. First-Principles calculations of the electronic structure and spectra of strongly correlated systems: The LDA+U method, J. Phys.: Condens. Matter **9**, 767 (1997).

[27] J. Heyd, G. E. Scuseria, and M. Ernzerhof, Hybrid functionals based on a screened Coulomb potential, J. Chem. Phys. **118**, 8207 (2003).

[28] A. Togo and I. Tanaka, First principles phonon calculations in materials science, Scr. Mater. **108**, 1 (2015).

[29] See Supplemental Material at http://link.aps.org/supplemental/10.1103/PhysRevB.97.094408 for electronic properties of MnX$_3$.

[30] P. V. Ong, N. Kioussis, P. K. Amiri, and K. L. Wang, Electric-field-driven magnetization switching and nonlinear magnetoelasticity in Au/FeCo/MgO heterostructures, Sci. Rep. **6**, 29815 (2016).

[31] M. Taherinejad, K. F. Garrity, and D. Vanderbilt, Wannier center sheets in topological insulators, Phys Rev B **89**, 115102 (2014).

[32] A. A. Mostofi, J. R. Yates, G. Pizzi, Y.-S. Lee, I. Souza, D. Vanderbilt, and N. Marzari, An updated version of WANNIER90: A tool for obtaining maximally-localised Wannier functions, Comput. Phys. Commun. **178**, 685 (2008).

[33] R. Yu, X. L. Qi, A. Bernevig, Z. Fang, and X. Dai, Equivalent expression of Z2 topological invariant for band insulators using the non-Abelian Berry connection, Phys. Rev. B **84**, 075119 (2011).

[34] D. Gresch, G. Autès, O. V. Yazyev, M. Troyer, D. Vanderbilt, B. A. Bernevig, and A. A. Soluyanov, Z2Pack: Numerical implementation of hybrid Wannier centers for identifying topological materials, Phys. Rev. B **95**, 075146 (2017).

[35] Q. Wu, S. Zhang, H.-F. Song, M. Troyer, and A. A. Soluyanov, WannierTools: An open-source software package for novel topological materials, Comput. Phys. Commun. **224**, 405 (2018).

[36] C. Z. Chang, J. Zhang, X. Feng, J. Shen, Z. Zhang, M. Guo, K. Li, Y. Ou, P. Wei, L. L. Wang, Z. Q. Ji, Y. Feng, S. Ji, X. Chen, J. Jia, X. Dai, Z. Fang, S.-C. Zhang, K. He, Y. Wang, L. Lu, X. C. Ma, and Q. K. Xue, Experimental observation of the quantum anomalous Hall effect in a magnetic topological insulator, Science **340**, 167 (2013).